ADVANCED ENERGY MATERIALS
www.advenergymat.de

Dual-Functional Atomic Zinc Decorated Hollow Carbon Nanoreactors for Kinetically Accelerated Polysulfides Conversion and Dendrite Free Lithium Sulfur Batteries

Haodong Shi, Xiaomin Ren, Jianmin Lu, Cong Dong, Jian Liu, Qihua Yang, Jian Chen, and Zhong-Shuai Wu**

The lithium sulfur (Li–S) battery is a preferential option for next-generation energy storage technologies, but the lithium polysulfide shuttling, sluggish redox kinetics, and uncontrollable lithium dendrite growth hamper its commercial viability. Herein, well-dispersed single atom Zn-decorated hollow carbon spheres (Zn_1-HNC) are developed as dual-functional nanoreactors for polysulfides-suppressed sulfur cathodes (Zn_1-HNC-S) and dendrite-free lithium anodes (Zn_1-HNC-Li) simultaneously for high-capacity, high-rate, and long-cycling Li–S batteries with fast redox kinetics. Benefiting from its excellent electronic conductivity, high surface area (370 m^2 g^{-1}), highly-effective active sites and protective carbon shell, the resultant nanoreactor possesses strong physical confinement, chemical anchoring, and exceptional electrocatalysis for polysulfides. Meanwhile, the nanoreactor with excellent lithiophilic ability realizes uniform and dendrite-free lithium deposition. Integrating all these advantages, the assembled full battery (Zn_1-HNC-S||Zn_1-HNC-Li) delivers remarkable electrochemical properties including long cycle stability with an ultralow capacity fading rate of 0.015% per cycle over 700 cycles and superb rate performance of 989 mAh g^{-1} at 10 C. Moreover, a high areal capacity of 8.7 mAh cm^{-2} with high S loading of 7.8 mg cm^{-2} at low E/S ratio (6.4 µL mg^{-1}) is achieved. This work provides significant insight of structure and surface catalytic chemistry regulation for promoting the actual application of Li–S batteries.

1. Introduction

The continuously growing demand for clean, sustainable power systems for consumer electronics, electric vehicles, and national grid storage is driving the research interest for electrochemical energy storage systems with better safety, lower cost, and higher energy density beyond current Li-ion battery.[1] Among alternative competitors, lithium sulfur (Li–S) battery has been considered as outstanding representative considering its high theoretical capacity (S: 1675 mAh g^{-1} and Li: 3860 mAh g^{-1}), sustainability of S, and lowest reduction potential of Li (−3.04 V vs SHE).[2] Despite intensive efforts over decades, the Li–S battery still suffers from several detrimental issues associated with both cathode and anode. For S cathode, the diffusion of intermediates lithium polysulfides (LiPS) and sluggish S redox conversion kinetic cause unsatisfactory specific capacity, inferior rate performance, and rapid capacity degradation.[3] For Li anode, the uncontrollable dendrite growth and infinite volume expansion result in safety risk and low Coulombic efficiency (CE).[4] Therefore, it is highly urgent to design the kinetically advanced Li–S battery system with well-designed configuration for both LiPS-suppressed cathode and dendrite-free anode.

Hollow carbon sphere nanoreactors with good electrical conductivity, large surface area, and enhanced structural stability have been widely applied as the host for secondary batteries to improve their electrochemical performance.[5] For example, as S cathode, a hollow porphyrin organic framework was designed for long cycling stability Li–S battery resulting from the physical confinement of LiPS.[6] Besides, double-shelled hollow carbon sphere was explored as a free-standing S host for high-energy-density Li–S battery.[7] As for Li anode, encapsulation of Li into the hollow carbon sphere was designed for high stable Li metal anode.[8] However, the shuttle effect and Li dendrite has not substantially been resolved because the physical effect only addresses the surface issue and not the root. To overcome this, integrating bare carbon nanostructures with catalysts, such as

---

H. D. Shi, X. M. Ren, C. Dong, Prof. J. Liu, Prof. Q. H. Yang, Prof. Z.-S. Wu
State Key Laboratory of Catalysis
Dalian Institute of Chemical Physics
Chinese Academy of Sciences
457 Zhongshan Road, Dalian 116023, China
E-mail: yangqh@dicp.ac.cn; wuzs@dicp.ac.cn
H. D. Shi, Dr. J. M. Lu, C. Dong, Prof. J. Chen, Prof. Z.-S. Wu
Dalian National Laboratory for Clean Energy
Dalian Institute of Chemical Physics
Chinese Academy of Sciences
457 Zhongshan Road, Dalian 116023, China
H. D. Shi, X. M. Ren, C. Dong
University of Chinese Academy of Sciences
19 A Yuquan Rd, Shijingshan District, Beijing 100049, China

The ORCID identification number(s) for the author(s) of this article can be found under https://doi.org/10.1002/aenm.202002271.

DOI: 10.1002/aenm.202002271

transition-metal sulfides,[9] oxides,[10] nitrides,[11] and nanoparticles,[12] not only guarantees the strong chemical interaction toward LiPS, but also catalytically promotes the rapid conversion of LiPS for S cathode. Furthermore, when these lithiophilic materials (Au, Zn, Sn) are applied in Li anode, a uniform Li deposition could be realized.[12] While these nanoreactors either suffer from heavy mass density, which is detrimental to high energy density of battery, or reduced conductivity and limited active sites for LiPS conversion and Li nucleation, therefore it is desirable for the development of a conductive lightweight nanoreactor with high-efficiency and well-dispersed active site.

Single atom catalysts with well-defined metal center not only possess promising electronic and reactive properties, but can also reach the theoretical 100% atomic utilization.[13] Thus, they have been used intensively in the area of energy storage and conversion.[14] In most cases of Li–S batteries, single atom has been anchored in an open structure, such as graphene,[15] mesoporous carbon,[16] or 2-methylimidazole zinc salt (ZIF)-derived carbon.[17] However, the open environment can not physically confine LiPS and prevent volume expansion of Li metal, but also decrease the loading of the S and Li. Taking into the above consideration, it is rational to introduce single atom catalysts into closed hollow carbon sphere nanoreactor to stabilize the single atom and act as a natural barrier against LiPS migration and Li dendrite.

In this work, we proposed single atom Zn modified hollow carbon sphere nanoreactor (Zn_1-HNC) as both S (Zn_1-HNC-S) and Li (Zn_1-HNC-Li) dual-functional hosts for kinetically enhanced, extremely stable, and high-rate Li–S full battery (Zn_1-HNC-S||Zn_1-HNC-Li). Such atomic level nanoreactor with well-dispersed atomic Zn possesses excellent electrical conductivity, high specific surface area (370 m^2 g^{-1}), and hierarchical porous structure, enabling the S cathode with enhanced S utilization, superior redox kinetics, strong physical confinement, and chemically catalytic conversion for LiPS. When employed as Li anode, uniform Li nucleation and suppressed dendritic growth are realized due to its excellent lithiophilic property. Consequently, the well-designed Li–S full battery shows excellent rate capability of 989 mAh g^{-1} at 10 C, and stable cycle life with an ultralow capacity decay rate of only 0.015% per cycle, as well as nearly 100% CE. Furthermore, the Zn_1-HNC-S||Zn_1-HNC-Li full cell delivers a high areal capacity of 8.7 mAh cm^{-2} at a high S areal loading of 7.8 mg cm^{-2} with a low electrolyte/sulfur ratio (E/S) of 6.4 µL mg^{-1}, negative/positive capacity ratio (N/P) of 1.8, demonstrating the great potential of Zn_1-HNC nanoreactor for high-energy-density Li–S battery.

2. Results and Discussion

2.1. Fabrication and Characterization of Zn_1-HNC Nanoreactor

The synthesis procedure of Zn_1-HNC-S cathode and Zn_1-HNC-Li anode for fabricating the Zn_1-HNC-S||Zn_1-HNC-Li full battery is illustrated in **Figure 1**. The dual-functional Zn_1-HNC nanoreactor with ultrahigh loading (15.7%) of single Zn atom is synthesized by pyrolysis of the hollow structured ZIF-8 precursor (Figure S1, Supporting Information) under Ar protection.[18] Notably, the Zn_1-HNC nanoreactor can simultaneously serve as an efficient electrocatalyst for S host (Zn_1-HNC-S) and excellent lithiophilic site for Li framework (Zn_1-HNC-Li). As a result, the formed Zn_1-HNC-S||Zn_1-HNC-Li full battery by combining the two advanced electrodes overcomes the challenges both of LiPS shuttling and Li dendrite growth for high-performance Li–S batteries, as discussed later.

The structural and morphology characterization of the as-prepared Zn_1-HNC are displayed in **Figure 2**. The Zn_1-HNC shows uniform hollow structure (≈300 nm, Figure 2a; Figure S2,

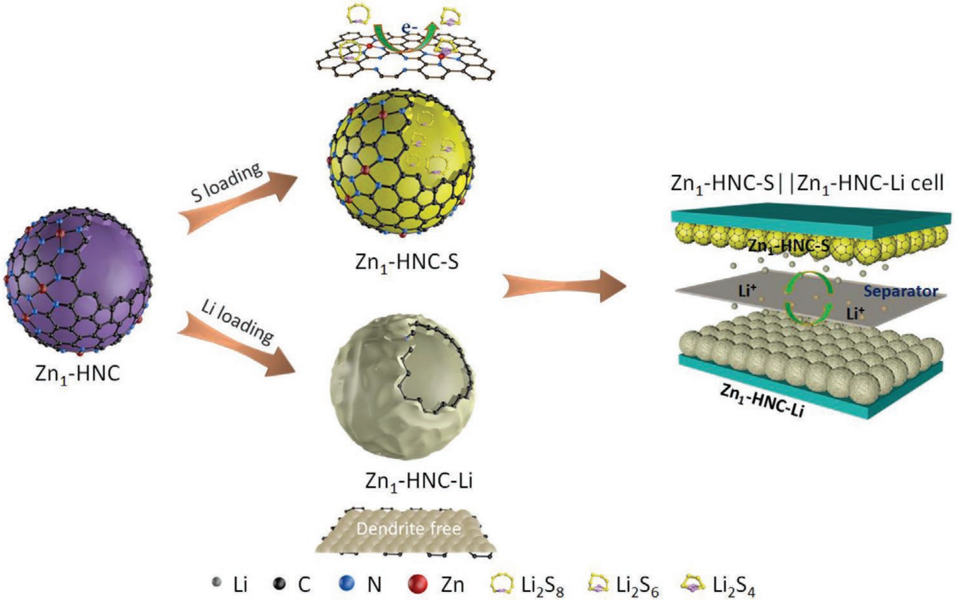

Figure 1. Synthesis schematic of the dual-functional Zn_1-HNC nanoreactors for Zn_1-HNC-S cathode and the Zn_1-HNC-Li anode of the Zn_1-HNC-S||Zn_1-HNC-Li full battery.

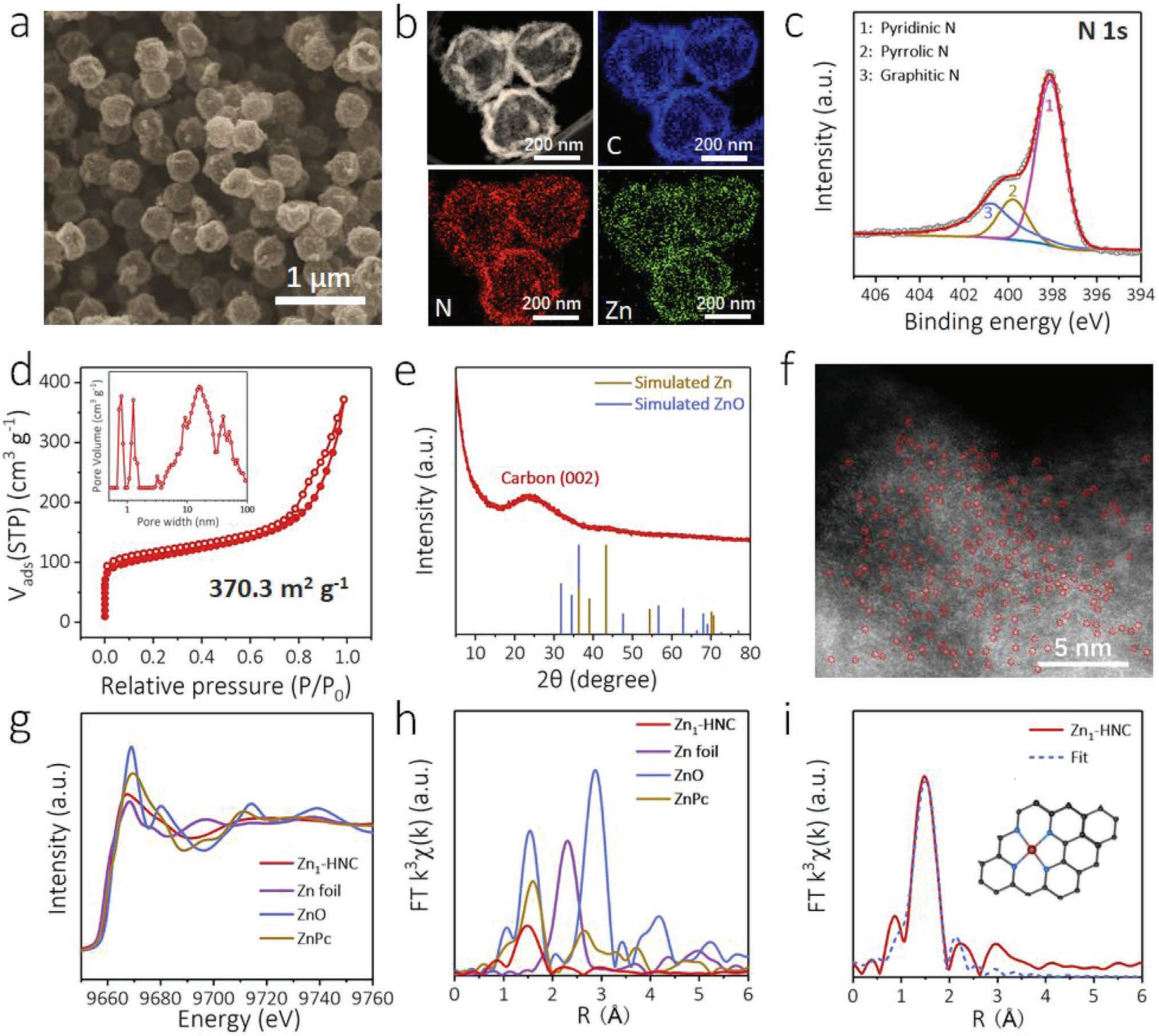

Figure 2. Morphology and structural characterizations of the as-prepared Zn$_1$-HNC. a) SEM image, b) HAADF-STEM image and corresponding elemental mapping images, and c) nitrogen adsorption–desorption isotherm of Zn$_1$-HNC. Inset is the pore size distribution of Zn$_1$-HNC. d) High-resolution XPS N 1s spectra, e) XRD pattern, and f) HAADF-STEM image of Zn$_1$-HNC, where the single Zn atoms present as red circles. g) Zn K-edge XANES and h) k^3-weighted Fourier transform of EXAFS spectra with respect to the reference samples. i) The EXAFS *R*-space fitting curve of Zn$_1$-HNC. Inset: schematic model of Zn$_1$-HNC, Zn red, N blue, and C gray.

Supporting Information) with uniform distribution of C, N, and Zn elements in the carbon shell (Figure 2b), which are further confirmed by the X-ray photoelectron spectroscopy (XPS) measurement (Figure S3, Supporting Information). The graphitic N (401.1 eV), pyrrolic N (399.7 eV), and pyridinic N (398.3 eV) of Zn$_1$-HNC can serve as the coordination sites for Zn atom (Figure 2c).[19] Notably, the high specific surface area (370 m^2 g^{-1}) and micro/meso hierarchical porous structure (≈1 and 15.9 nm) are beneficial to enhance the S loading and offer facile accessibility of the active sites for LiPS adsorption and conversion reactions (Figure 2d).[20] X-ray diffraction (XRD) pattern indicates the absence of Zn or ZnO aggregates in the Zn$_1$-HNC (Figure 2e), which is consistent with TEM result (Figure S4, Supporting Information). The Zn content is as high as 15.7% confirmed by inductively coupled plasma analysis, which is among the highest level in the reported single atom Zn based catalysts.[18] To further visualize the nature of Zn single atoms, the atomic-resolution aberration-corrected resolution high-angle annular dark field-scanning transmission electron microscopy (HAADF-STEM) was performed. The individual Zn atoms are homogeneously dispersed in the carbon shell of Zn$_1$-HNC (seen as bright circles), demonstrating the successful creation of monodispersed single-atom electrocatalyst in Zn$_1$-HNC (Figure 2f; Figure S5, Supporting Information). To elucidate the electronic structure and chemical configuration of Zn atom in Zn$_1$-HNC, X-ray absorption near edge structure

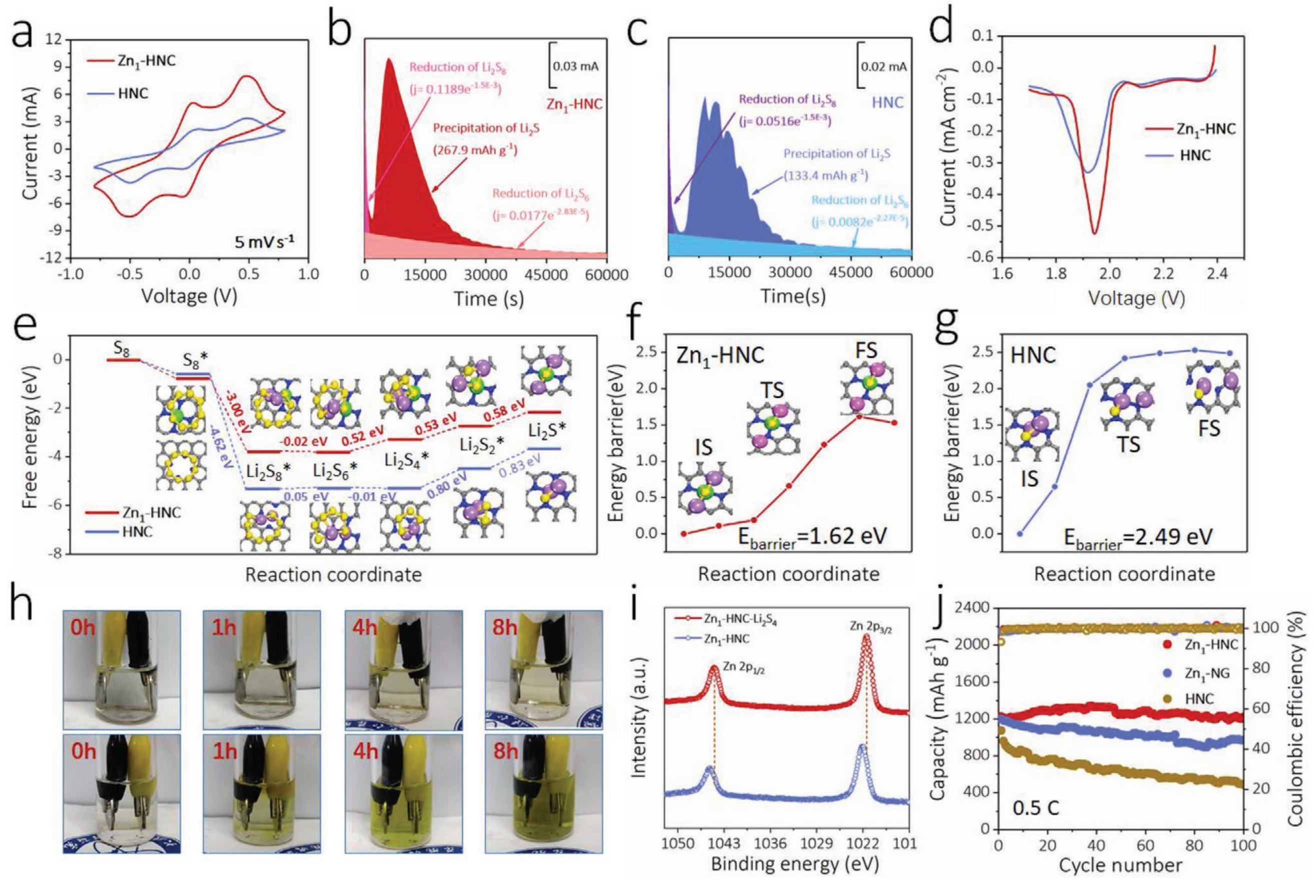

Figure 3. Electrocatalytic conversion and adsorption effects of Zn$_1$-HNC on LiPS. a) CV curves of Li_2S_6 symmetric cells employing Zn$_1$-HNC or HNC at 5 mV s^{-1}. Potentiostatic discharge curves of a Li_2S_8/tetraglyme solution at 2.05 V on b) Zn$_1$-HNC and c) HNC. d) LSV analyses of Zn$_1$-HNC and HNC electrodes with Li_2S_4 catholyte. e) Energy profiles for the reduction of LiPS on Zn$_1$-HNC and HNC substrates (yellow ball: S atom; purple ball: Li atom; grey ball: C atom; green ball: Zn atom; blue ball: N atom). The decomposition energy barriers of Li_2S on the f) Zn$_1$-HNC and g) HNC electrodes (IS: initial structure, TS: transition structure, and FS: final structures). h) Visual illustration of polysulfide entrapment at different discharge process by Zn$_1$-HNC-S (top) and HNC-S (bottom) cathode based Li–S batteries. i) XPS Zn 2p spectra of Zn$_1$-HNC before and after adsorption of Li_2S_4. j) Cycling performance and CE of the Li–S batteries with Zn$_1$-HNC, Zn$_1$-NG, and HNC measured at 0.5 C for 100 cycles.

(XANES) and the extended X-ray absorption fine structure (EXAFS) of Zn K-edge were carried out. The absorption edge position of Zn$_1$-HNC is located between those of the metallic Zn foil (Zn^0) and the ZnPc (Zn^{2+}), indicating a positive charge on Zn atom with average valence state between 0 and +2 (Figure 2g). The EXAFS spectrum of *R* space for Zn$_1$-HNC shows a main peak of Zn–N coordination at 1.47 Å, and no Zn–Zn coordination peak in Zn foil (2.3 Å) and ZnO (2.9 Å) is detected, implying that Zn atom is mainly dispersed as single atoms on this carbon shell (Figure 2h). According to the EXAFS fitting, Zn-N$_4$ is the dominant coordination mode of Zn atoms in Zn$_1$-HNC (Figure 2i; Table S1, Supporting Information).

2.2. Electrocatalytic and Adsorption Effects of Zn$_1$-HNC on LiPS

To demonstrate the electrocatalytic activity regarding liquid–liquid conversion process of single atom Zn, Li_2S_6 symmetric cells were first assembled using Zn$_1$-HNC or bare HNC electrodes as both anode and cathode. Notably, the symmetric cells with Zn$_1$-HNC electrode show higher response current with obvious redox peaks compared to HNC electrode (**Figure 3**a), suggesting that Zn$_1$-HNC possessed better electrochemical kinetics for LiPS conversion (Figure S6, Supporting Information). The solid–liquid conversion experiment was carried out on Zn$_1$-HNC and HNC electrodes surface to understand the kinetics of Li_2S nucleation. Figure 3b,c exhibit the potentiostatic discharge curves of the aforementioned electrodes at 2.05 V. The Zn$_1$-HNC shows a much higher and earlier discharging current peak (0.14 mA at 6018 s) than the HNC (0.05 mA at 11 860 s). Additionally, the capacity of Li_2S precipitation on Zn$_1$-HNC (267 mAh g^{-1}) is much higher than HNC (133 mAh g^{-1}), indicting the accelerated liquid–solid transformation process on the Zn$_1$-HNC surface, so that the capacity and cycle stability of Li–S batteries would be kinetically enhanced.[21] Furthermore, the catalytic effect of Zn$_1$-HNC was verified by the linear sweep voltammetry (LSV) measurement in the Li_2S_4 catholyte. The Zn$_1$-HNC electrode shows higher reaction current peak (–0.52 mA cm^{-2}) and decreased Tafel slopes (107 mV dec^{-1}) than that of HNC (–0.33 mA cm^{-2}, 160 mV dec^{-1}) (Figure 3d; Figure S7, Supporting Information), further validating the enhanced kinetics of LiPS redox reaction by the atomic Zn sites within the HNC.[22] Density functional theory (DFT) calculation was further adopted for investigating the mechanism of the adsorption and catalytic effects of LiPS on Zn_1-HNC surface (Figure S8, Supporting Information). Figure 3e shows the calculated free energy of the stepwise disproportionation products including S_8, Li_2S_8, Li_2S_6, Li_2S_4, Li_2S_2, and Li_2S on the Zn_1-HNC and HNC during the S conversion reaction. The reduction of Li_2S_2 to Li_2S has the highest positive Gibbs free energy in the whole discharging process, demonstrating that it is the rate-limiting step in the Li–S battery.[23] And the value on Zn_1-HNC (0.58 eV) is much lower than HNC (0.83 eV), suggesting that the S reduction is thermodynamically more favorable on Zn_1-HNC than HNG. In the inverse charging process, Li_2S decomposition is the first step (Table S2, Supporting Information). The Li_2S decomposition energy barrier of Zn_1-HNC surface (1.62 eV) is far lower than that of HNC (2.49 eV), which confirms that the single Zn atom in HNC efficiently catalyzes the breaking of the Li—S bond to accelerate reaction kinetics of delithiation in electrochemical process (Figure 3f,g).[15d]

High absorptivity with LiPS is prerequisite for improving the heterocatalytic capacity between LiPS and solid electrocatalysis.[24] The strong surface affinity of Zn_1-HNC for LiPS was directly evidenced by the in situ visual experiments. The transparent electrolyte quickly changes to yellow (1 h) due to the overflow of LiPS of HNC-S electrode, in sharp contrast to the unchanged electrolyte color (8 h) around the Zn_1-HNC-S cathode, indicative of the strong immobilization of LiPS by Zn_1-HNC (Figure 3h). Furthermore, the yellow Li_2S_4 (7 mmol L^{-1}) electrolyte becomes colorless after soaking Zn_1-HNC (5 mg) for 12 h in the static adsorption experiments, consistent with the UV–vis spectra results, suggesting more adsorbing sites of Zn_1-HNC than HNC (Figure S9, Supporting Information). The high-resolution Zn 2p XPS spectrum shows a clear shift to low binding energies after Li_2S_4 adsorption (0.6 eV) and formation of obvious Zn—S bond (Figure 3i; Figure S10, Supporting Information), confirming the intense interaction of exposed Zn site with Li_2S_4 species in the electrolyte. It should be stressed that different from that reported to date for single atom LiPS catalysts, such as graphene-single atom cobalt,[15a] mesoporous carbon-single atom cobalt,[16] and graphene-single atom nickel,[25] the Zn_1-HNC nanoreactors not only possess high catalytic activity for the LiPS, but also physically confine LiPS into the hollow shell well, so that a high S loading with longer cycle stability of Li–S battery could be realized.[26] To prove this, single atom Zn (≈1 wt%) on nitrogen-doped graphene (Zn_1-NG) was synthesized for comparison (Figure S11, Supporting Information). As expected, Zn_1-HNC possesses better electrochemical capability for LiPS than Zn_1-NG due to their more effective active sites (Figure S12, Supporting Information). Significantly, Zn_1-HNC can achieve a high S loading of 80% (Figure S13, Supporting Information), in which the nano-sulfur is well confined in the hollow shell without big S particles observed (Figure S14, Supporting Information). When tested in Li–S batteries with the prepared S cathode, the Zn_1-HNC-S cathode, with the lowest interfacial impedance of 40 Ω (110 Ω for Zn_1-NG and 301 Ω for HNC-S) and an Li ion diffusion coefficient of 1.96×10^{-13} cm^2 s^{-1}, exhibits the higher initial discharged capacity (1225 mAh g^{-1}) than those of Zn_1-NG-S (1178 mAh g^{-1}) and HNC-S (1075 mAh g^{-1}) at 0.5 C (Figures S15,S16, Supporting Information). After 100 cycles, Zn_1-HNC-S cathode maintains a capacity of 1214 mAh g^{-1} with CE ≈ 100%, corresponding to an extremely low average capacity decay rate of ≈0.009% per cycle, which is much lower than those of Zn_1-NG-S (0.21%) and HNC-S (0.54%) (Figure 3j; Figure S17, Supporting Information). In addition, Zn_1-HNC shows highly reversible Li_2S_2 and Li_2S deposition and resolvation during discharge and charge process (Figure S18, Supporting Information). These results strongly confirm the great advantages of Zn_1-HNC nanoreactors as high-loading sulfur cathodes with stimulative reaction kinetics for high performance Li–S batteries.

2.3. Lithium Dendrite Suppression of Zn_1-HNC

Considering that practical use of Li—S batteries is also limited with the unwanted dendrite-growth of Li anode,[27] Zn_1-HNC is expected as an advanced material to achieve dendrite-free Li anode. DFT calculations demonstrate that Li adsorption energy of −2.04 eV on Zn_1-HNC is bigger than that on the bare carbon (−0.48 eV) (**Figure 4**a), and the Li atom prefers to nucleate around the single Zn atom based on the charge density difference analysis (Figure 4b; Figure S19, Supporting Information), indicating Zn_1-HNC sufficient provision of Li nucleation sites for uniform Li nucleation. After precycling between 0.01 and 3 V for five times to stabilize SEI film (Figure S20, Supporting Information), CE was first tested to evaluate the reversibility of different Li electrodes. The Zn_1-HNC exhibits a significantly higher and stable CE (99.9% for 100 cycles) than HCN (93% for 109 cycles), super P carbon (SP, 93% for 67 cycles), and bare Cu electrodes (82% for 8 cycles) at 1 mA cm^{-2} with capacity of 1 mAh cm^{-2} (Figure 4c; Figure S21, Supporting Information). Moreover, the voltage curve of Zn_1-HNC electrode shows a smooth voltage dip with an ultralow overpotential of only 15 mV, which is much smaller than that of HCN (37 mV), SP (39 mV), and bare Cu substrate (201 mV). This is a further proof of the high lithiophilic property of the Zn_1-HNC for facilitating Li nucleation.[28] When the cycling capacity increased to 6 mAh cm^{-2} at 3 mA cm^{-2}, the Zn_1-HNC electrode still reaches a high CE (98.7%) after 100 cycles (Figure S22, Supporting Information). The Zn_1-HNC electrode also exhibits excellent rate capability at constant current of 1 mA cm^{-2} with Li capacities up to 9 mAh cm^{-2} (Figure S23, Supporting Information) and constant plating time for 1 h so far as to an increased current density of 7 mA cm^{-2} (Figure S24, Supporting Information), suggesting the outstanding Li utilization and reversibility of Zn_1-HNC electrode. The Li plating/stripping performance was further studied by Li—Li symmetrical batteries. Notably, the excellent cycling stability (1200 h) with overpotentials of around 16 mV is realized for symmetric Zn_1-HNC-Li batteries at a current density of 3 mA cm^{-2} with a plating/striping time of 1h. In a stark contrast, a limited cycling life with fluctuating voltage hysteresis is observed for SP–Li (42 mV for 400 h) and Cu–Li electrode (110 mV for 100 h) (Figure 4e,f; Figure S25, Supporting Information). The distinctively decreased polarization and impressive cycle stability can be further verified by the electrochemical impedance spectroscopy (EIS). The R_{SEI} (representative of Li ion-diffusion kinetics of the formed SEI film)

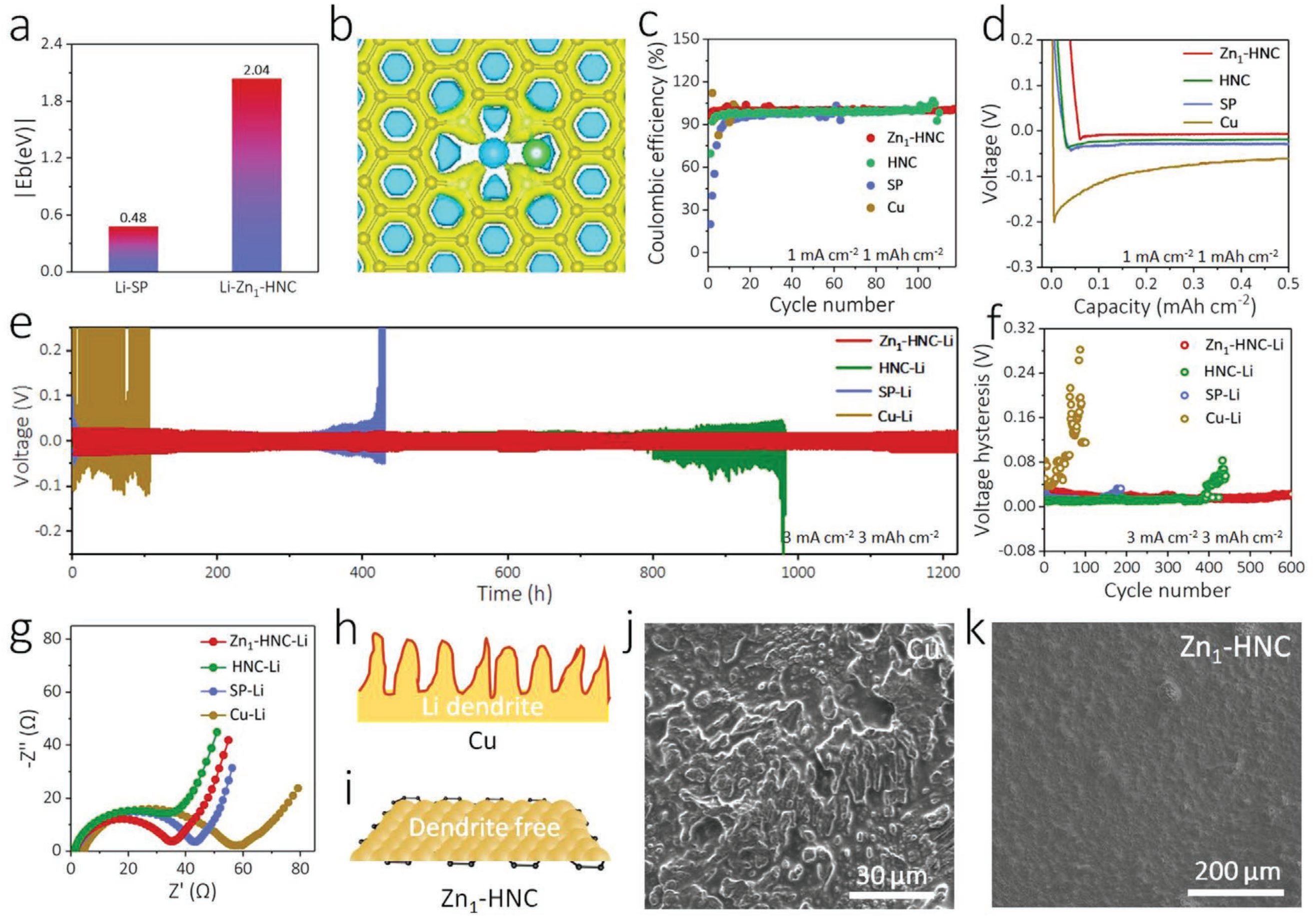

Figure 4. Lithium dendrite suppression of Zn_1-HNC. a) Binding energy of a Li atom with Zn_1-HNC and SP. b) The deformation charge density at an Li atom adsorption site of Zn_1-HNC. c) CE and d) enlarged plating-stripping curves of Zn_1-HNC, HCN, SP, and Cu foil electrodes at current density of 1 mA cm^{-2} with the capacity of 1 mAh cm^{-2}. e) Galvanostatic cycling of symmetric cells based on Zn_1-HNC-Li, HCN-Li, SP-Li, and Cu-Li electrodes at current density of 3 mA cm^{-2} under stripping/plating capacity of 3 mAh cm^{-2}, and f) corresponding voltage hysteresis variation with cycling number, and g) Nyquist plots obtained after 100 cycles. Schematic illustration of the electrochemical deposition behaviors of the h) Cu and i) Zn_1-HNC electrodes. Top-view SEM images of j) Cu and k) Zn_1-HNC electrodes with Li deposition capacities of 0.25 mAh cm^{-2}.

of Zn_1-HNC-Li electrode (35 Ω) is much smaller than those of HNC–Li (40 Ω), SP–Li (45 Ω), and Cu–Li electrode (57 Ω), indicating the formation of a stable and high ion-conducing SEI film in the Zn_1-HNC-Li electrode.[29] To clarify the Li deposition behavior of the Zn_1-HNC-Li electrode, the surface morphology of the anodes was observed by SEM. Unlike the uneven deposition and undesirable Li dendrite on the surface of bare Cu electrode (Figure 4h,j), with homogenous Zn single atom lithiophilic site of Zn_1-HNC, ultrafine and smooth Li nucleation is realized (Figure 4i,k; Figure S26, Supporting Information). The differences of the Li deposition process between bare Cu and Zn_1-HNC highlight the advantages of Zn_1-HNC in the improvement of Li electrochemistry performance, which is promising to further promote the Li—S battery performance.

2.4. Performance of Zn_1-HNC-S||Zn_1-HNC-Li Full Battery

Based on well-designed properties of the dual-functional nanoreactors for both the cathode and the anode, the developed Zn_1-HNC-S cathode and Zn_1-HNC-Li anode were coupled as an Li–S full battery (denoted as Zn_1-HNC-S||Zn_1-HNC-Li) to investigate the comprehensive improvement of electrochemical performance. An SP-S||Li battery was also assembled as a control. Notably, the Zn_1-HNC-S||Zn_1-HNC-Li full battery realizes a higher initial capacity of ≈1111 mAh g^{-1} than that of SP-S||Li cell (972 mAh g^{-1}) at 1 C. In addition, a stable discharge capacity of 1149 mAh g^{-1} is retained over 300 cycles for Zn_1-HNC-S||Zn_1-HNC-Li, while only 60% (590 mAh g^{-1}) capacity can be kept for SP-S||Li battery, demonstrating the higher S utilization and more stable electrode structure of both anode and cathode of Zn_1-HNC-S||Zn_1-HNC-Li (**Figure 5**a,b; Figure S27, Supporting Information). Moreover, the self-discharge phenomenon is also efficiently suppressed by using these two advanced electrodes with a stable open circuit voltage (2.4 V) for 45 h (Figure S28, Supporting Information). More importantly, the obtained Li–S full battery shows superior rate performance with a highly reversible capacity of 989 mAh g^{-1} and high CE ≈ 100% at an ultrahigh rate of 10 C. Remarkably, the ultrahigh rate performance has rarely reported in the former work, such as

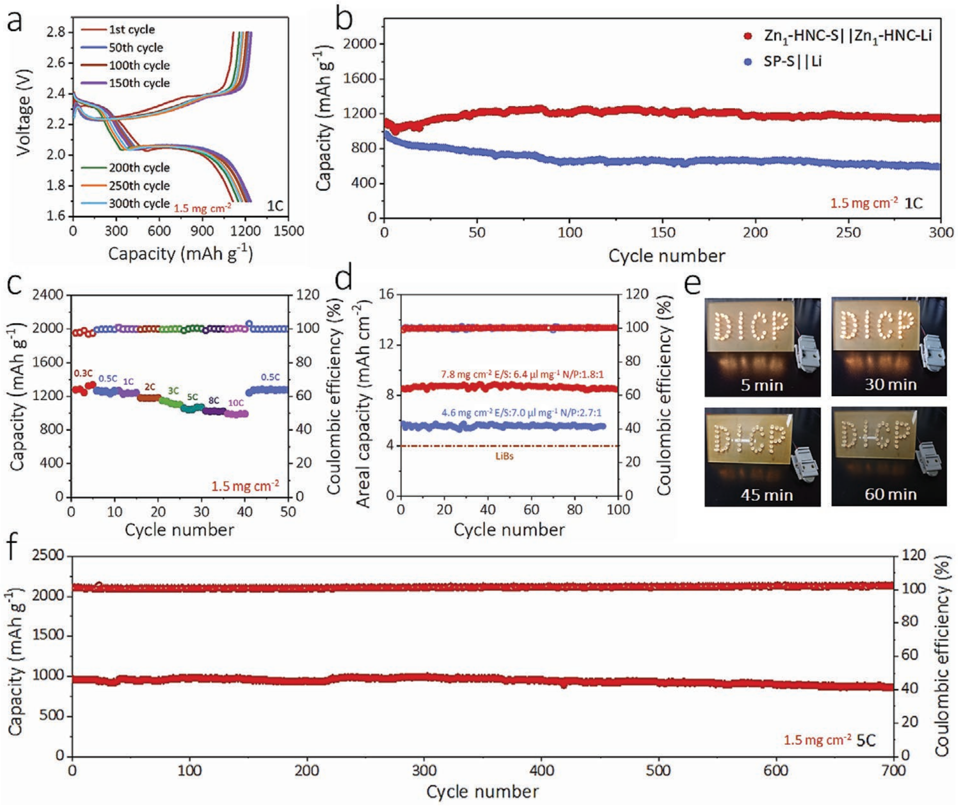

Figure 5. Electrochemical performance of Zn_1-HNC-S||Zn_1-HNC-Li full battery. a) Galvanostatic charge and discharge curves obtained at different cycles of Zn_1-HNC-S||Zn_1-HNC-Li battery. b) Cycling stability for 300 cycles tested at 1.0 C (1.0 C = 1675 mAh g^{-1} for S anode) of Zn_1-HNC-S||Zn_1-HNC-Li and SP-S||Li batteries. c) Rate capability of Zn_1-HNC-S||Zn_1-HNC-Li batteries. d) Areal capacity of Zn_1-HNC-S||Zn_1-HNC-Li batteries obtained at 0.5 C with high sulfur loading of 4.6 and 7.8 mg cm^{-2}, respectively. e) Photograph of LED lit by Zn_1-HNC-S||Zn_1-HNC-Li battery at different time. f) Long-term cycling stability of 700 cycles and corresponding CE of Zn_1-HNC-S||Zn_1-HNC-Li batteries measured at 5 C.

VN–S (910 mAh g^{-1} at 4 C),[30] graphene–S (713 mAh g^{-1} at 10 C),[31] illustrating the fast reaction kinetics (Figure 5c; Figure S29, Supporting Information). The maximum specific power density (13 325 W kg^{-1}) and energy density (1793 Wh kg^{-1}) calculated based on the mass of Zn_1-HNC-S cathode is competitive to most previous reports (Figure S30, Supporting Information), such as graphene–S (2095 W kg^{-1}, 1308 Wh kg^{-1}),[31] graphite foam–S (9583 W kg^{-1}, 1613 Wh kg^{-1}),[32] and cobalt in nitrogen-doped graphene–S (3540 W kg^{-1}, 1715Wh kg^{-1}).[15a] In addition, since the S areal loading and E/S ratio are considered as the critical parameters for the practical application, a high S areal loading of 4.6 and 7.8 mg cm^{-2}, corresponding to E/S of 7.0 and 6.4 µL mg^{-1}, N/P of 2.7:1 and 1.8:1, respectively, were assembled to further demonstrate the superiority of the Zn_1-HNC-S||Zn_1-HNC-Li full battery. As shown in Figure 5d, an areal capacity of 5.6 and 8.7 mAh cm^{-2} was realized with superior cycling stability around 100 cycles and CE of nearly 100% at 4.6 and 7.8 mg cm^{-2}, respectively, which far outperformed conventional Li-ion batteries (4 mAh cm^{-2}) and the most of high S loading cathodes reported recently (Figure 5d; Table S3, Supporting Information), such as VS_2-graphene (5.0 mg cm^{-2}, 4.0 mAh cm^{-2}, 50 cycles),[33] TiN (4.6 mg cm^{-2}, 3.15 mAh cm^{-2}, 50 cycles),[34] and CNT (6.3 mg cm^{-2}, 5.0 mAh cm^{-2}, 60 cycles).[35] Encouragingly, the as-assembled Zn_1-HNC-S||Zn_1-HNC-Li cell successfully powers a yellow LED for 1 h, indicating the hopeful potential in practical application (Figure 5e). The long cyclability of Zn_1-HNC-S||Zn_1-HNC-Li full battery was also tested at 5 C, showing a high specific capacity of 963 mAh g^{-1} with ultralow damping rate of only 0.015% each cycle after 700 cycles (Figure 5f; Figure S31, Supporting Information) that is well comparable with the state-of-the-art high-performance carbon-based Li–S batteries (Table S4, Supporting Information) and superior to all the reported single atom catalysts for Li–S batteries (Table S5, Supporting Information). Overall, the excellent performance of the full battery indicates the great potential of the nanoreactor Zn_1-HNC based Li–S full battery for high-energy-density energy storage devices.

3. Conclusion

In summary, we developed high-capacity, high-rate, and long-cycling Li–S full batteries by employing hollow carbon spheres anchored with single atom Zn (Zn_1-HNC) as a dual-functional nanoreactor for shuttling-inhibition S cathode and dendrite-free Li anode simultaneously. Owing to the massive homogeneously dispersed single atom clusters, excellent electrical conductivity, and abundant porous structure, the utilization, confinement, and redox kinetics of the LiPS have been remarkably enhanced, as well as uniform Li stripping/plating with significantly suppressed dendrite growth is realized. As a consequence, the fabricated Li–S full battery (Zn$_1$-HNC-S||Zn$_1$-HNC-Li) shows outstanding rate capability (989 mAh g^{-1} at 10 C) and long cycle stability (700 cycles at 5 C with ultralow capacity decay ≈ 0.015% per cycle) with almost 100% CE. Even at high S areal loading of 7.8 mg cm^{-2} with a low E/S ratio of 6.4 µL mg^{-1}, N/P of 1.8:1, a high areal capacity of 8.7 mAh cm^{-2} still can be realized for Zn$_1$-HNC-S||Zn$_1$-HNC-Li full battery can still deliver. Therefore, this atom-level designed nanoreactors offer a clear avenue to settle the obstacles of LiPS-suppressed cathode and dendrite-free anode for the exploitation of safer, high-energy-density, and long cycle life Li-metal batteries.

4. Experimental Section

Preparation of Zn$_1$-HNC: Zn$_1$-HNC was prepared as previously reported.[18] Typically, 150 mg carboxylate-terminated polystyrene (PS),[36] 0.8 g 2-methylimidazole, and 300 mg Zn(NO$_3$)$_2$·6H$_2$O were mixed in 40 mL methanol and stirred at 70 °C for 1 h. Then, the solid product was separated by centrifugation and washed, followed by drying overnight at 60 °C. Once dried, the solid was immersed in dimethylformamide to remove the PS cores. Finally, the obtained product was carbonized at 800 °C for 2 h under Ar atmosphere, resulting in the Zn$_1$-HNC.

Preparation of HNC: First, 25 mg Zn$_1$-HNC was stirred in 10 mL HCl (1 м) at 80 °C for 5 h. The formed solid was washed with de-ionized water to remove the residual acid, and then dispersed in NaOH (1 м) and stirred at 80 °C for 5 h, followed by centrifugation and washing with deionized water three times. Finally, the sample was etched in a mixed solution of 4 mL H$_2$O and 1 mL HF at 80 °C for 5 h. The resulting product was collected by centrifugation three times with methanol and further dried at 60 °C under vacuum.

Preparation of Zn$_1$-NG: GO was synthesized by the modified Hummer's method.[37] 10 mL Zn(NO$_3$)$_2$·6H$_2$O (1 mg mL^{-1}) aqueous solution was added dropwise into 100 mL GO suspension (1 mg mL^{-1}) under vigorous sonication and sonicated for another 30 min, followed by rapid freezing in liquid nitrogen. The precursor was freeze-dried at –70 °C. The dried precursor was then heated at a rate of 3 °C min^{-1} up to 450 °C under Ar atmosphere for 6 h.

Synthesis of Zn$_1$-HNC-S, HNC-S, and Zn$_1$-NG Composite: The Zn$_1$-HNC-S composite was prepared via the classical melt-diffusion method. The Zn$_1$-HNC powder was mixed with required elemental sulfur (4:1 by mass) thoroughly by grinding. Then, the obtained powder was annealed at 155 °C for 12 h under Ar atmosphere. For comparison, HNC-S and Zn$_1$-NG-S composite was prepared in the same way as Zn$_1$-HNC-S.

Visualized Adsorption of Polysulfides: Li$_2$S$_4$ solution was prepared by mixing sulfur particles and Li$_2$S with a molar ratio of 3:1 in 1,2-dimethoxyethane (DME) solution in an Ar-filled glovebox followed by intense stirring for 24 h. The concentration of Li$_2$S$_4$ was 5.0 mmol L^{-1}. Zn$_1$-HNC and HNC with the same mass (1 mg) were added to 1.0 mL of Li$_2$S$_4$/DME solution, respectively. After the mixtures were kept standing for 12 h, the digital photographs were taken. The supernatant and the Zn$_1$-HNC precipitates were studied by UV–vis spectrophotometry and XPS, respectively.

Assembly of Symmetric Cells and Kinetic Evaluation of Polysulfide Conversion: The Zn$_1$-HNC (or HNC) powder was mixed with polyvinylidene fluoride (PVDF) binder with a weight ratio of 4:1 and then coated on the Al foil and dried at 120 °C for 12 h. The electrodes were obtained with an average mass loading of 1 mg cm^{-2} for both Zn$_1$-HNC and HNC. The electrodes were used as both working and counter electrode, and 40 µL catholyte (0.5 м Li$_2$S$_6$ and 1.0 м solution of lithium bis[trifluoromethanesulfonyl]imide (LiTFSI) with 1 wt% LiNO$_3$ in 1,3-dioxolane (DOL) and DME, v/v = 1:1) was added into each coin cell. The CV measurement of the symmetric cell was conducted at a scan rate of 5 mV s^{-1} with a voltage window between –0.8 and 0.8 V.

Measurement for Li$_2$S Nucleation: Nucleation of Li$_2$S on different electrodes were probed in standard 2016 coin cells with 20 µL Li$_2$S$_8$ tetraglymesolution (0.2 mol L^{-1} based on sulfur) as catholyte and 20 µL of control electrolyte without Li$_2$S$_8$ was used as anolyte. Li foil was employed as the anode, Zn$_1$-HNC and HNC electrodes used in the kinetic study served as the working electrode. The assembled cells were first discharged galvanostatically at 0.112 mA to 2.06 V and then discharged potentiostatically at 2.05 V for Li$_2$S nucleation and growth until the current dropped below 10^{-5} A. It took about 60 000 s and the energy was integrated to evaluate the capacities from deposition of lithium sulfide on various surfaces according to Faraday's law.

Material Characterization: The morphology and structure of materials and electrodes were characterized by SEM (JEOL JSM-7800F), TEM (JEM-2100), HRTEM (JEOL 2100), aberration-corrected HAADF-STEM (FEI Titan Cube Themis G2 300, 300 kV equipped with two spherical aberration correctors), XPS (Thermo ESCALAB 250Xi equipped with monochromatic Al Kα source of 1486.5eV), XRD (Empyrean with Cu Kα radiation in the 2θ range from 5° to 90°), nitrogen adsorption and desorption isotherm (Quadrasorb SI). The Zn K-edge EXAFS data were collected on the beamline BL14W1 at Shanghai Synchrotron Radiation facility (SSRF).

Electrochemical Measurement: The sulfur composite cathodes were prepared by mixing the as-prepared samples (Zn$_1$-HNC-S, Zn$_1$-NG-S, or HNC-S), acetylene black, and binder (PVDF) in *N*-methyl-pyrrolidinone solvent with a weight ratio of 8:1:1. The resulting homogeneous slurry was coated onto the current collector (12 mm diameter carbon coated Al foil), followed by drying at 60 °C for 24 h. CR-2016 coin cells were assembled in an argon-filled glove box using the Zn$_1$-HNC-S, Zn$_1$-NG-S, or HNC-S as the cathode, a porous membrane (Celgard 2400) sheets as the separator, and Li foil as the counter electrode. A 1.0 м solution of LiTFSI with 1 wt% LiNO$_3$ in DOL and DME (v/v = 1:1) was used as the electrolyte. The as-obtained Zn1-HNC, HNC or SP as active materials and PVDF as binder (mass ratio of active materials: binder = 9:1) were mixed into a slurry by stirring in N-methyl-2-pyrrolidone. Then the slurry was coated onto Cu foil and dried in a vacuum drying oven at 100 °C for 12 h. Further, the foil was punched into the disks as the working electrode. The loading mass of materials was approximately ~1 mg cm^{-2}, and bare Cu foil was also punched for reference. All the batteries were assembled with standard CR2016 coin-type batteries in an argon-filled glovebox with O$_2$ and H$_2$O content below 0.5 ppm. The electrolyte 1.0 м LiTFSI in a mixture solution of DOL and DME (1:1, vol. ratio) with 1 wt% LiNO3 as additive. About 40 µL electrolyte was dropped into each battery. Zn$_1$-HNC, HNC, SP or bare Cu electrodes severed as the working electrodes, and Li metal was used as the counter/reference electrodes to evaluate the CE. The assembled batteries were precycled between 0.01 and 3 V for 5 times to stabilize the SEI formation and remove surface contaminations. Afterwards, a certain capacity of Li was deposited onto the electrodes and then charged to 1 V (vs Li+/Li) to strip the Li at certain current density for each cycle on a LAND CT2001A battery system. And symmetric batteries configurations were assembled with Zn$_1$-HNC-Li, HNC-Li, SP-Li or pure Li anodes to evaluate the long-time cycling stability. Zn$_1$-HNC-S||Zn$_1$-HNC-Li full cells were assembled by using Zn$_1$-HNC-S as cathode and Zn$_1$-HNC-Li as anode. The average mass of S cathode used in this work were controlled around 1.5 mg cm^{-2}, corresponding to 1.6 mAh cm^{-2}. For high S loading test, 4.6 and 7.8 mg cm^{-2} areal loading S were also prepared. The Zn$_1$-HNC-Li anodes were prepared by pre-plating Li into Zn$_1$-HNC with excessive Li of 15 mAh cm^{-2}, the N/P was about 9.4:1. The common electrolyte/sulfur ratio was fixed at 15 µL mg^{-1}. The performances of Li–S batteries were measured on an LANDCT2001A analyzer under different current rates at a voltage interval from 1.7 to 2.8 V. The cyclic voltammograms (CV) curves were collected on a CHI-760E electrochemical workstation (Chenhua Instrument, Shanghai) at a scan rate of 0.1 mV s^{-1}. EIS analysis was carried out in the range of 100 kHz to 0.01 Hz.

Computational Simulation: Vienna Ab Initio Package (VASP)[38] was employed the to perform all the DFT calculations within the generalized gradient approximation using the PBE[39] formulation. Projected augmented wave potentials[40] were chosen to describe the ionic cores and take valence electrons into account using a plane wave basis set with a kinetic energy cutoff of 400 eV. Partial occupancies of the Kohn–Sham orbitals were allowed using the Gaussian smearing method and a width of 0.05 eV. The electronic energy was considered self-consistent when the energy change was smaller than 10^{-7} eV. A geometry optimization was considered convergent when the energy change was smaller than 10^{-6} eV. The spin polarization was considered in all calculations.

The equilibrium lattice constant of hexagonal graphene unit cell was calculated, when using a gamma-point centered $15 \times 15 \times 11$ k-point grid for Brillouin zone sampling, to be $a = b = 2.4680$ Å, which was in accord with the experimental one. This unit cell was used to construct the monolayer graphene with a p (7×7) periodicity in the x, y directions, separated by a 15 Å of vacuum in the z direction between the graphene and its periodic images. The gamma k-point in the Brillouin zone was used in the following surface calculations. During structural optimizations, all atoms were allowed to fully relax.

The adsorption energy of an Li atom was defined as

$$E_{\mathrm{ads}} = E_{\mathrm{Li/surf}} - E_{\mathrm{surf}} - E_{\mathrm{Li}} \tag{1}$$

where $E_{\mathrm{Li/surf}}$, E_{surf}, and E_{Li} are the energy of the Li adsorbed on the graphene surface, the energy of graphene clean surface, and the energy of isolated Li atom in a cubic box with side length of 15 Å, respectively.

The transition state of an elementary reaction step was located by the nudged elastic band (NEB) method.[41] In the NEB method, the path between the reactant(s) and product(s) was discretized into a series of five structural images.

Supporting Information

Supporting Information is available from the Wiley Online Library or from the author.

Acknowledgements

H.D.S., X.M.R., and J.M.L. contributed equally to this manuscript. This work was financially supported by the National Key R&D Program of China (Grant 2016YBF0100100), National Natural Science Foundation of China (Grants 51872283, and 21805273), Liaoning BaiQianWan Talents Program, LiaoNing Revitalization Talents Program (Grant XLYC1807153), Natural Science Foundation of Liaoning Province, Joint Research Fund Liaoning-Shenyang National Laboratory for Materials Science (Grant 20180510038), DICP (DICP ZZBS201708, DICP ZZBS201802, and DICP I202032), DICP&QIBEBT (Grant DICP&QIBEBT UN201702), Dalian National Laboratory For Clean Energy (DNL), CAS, DNL Cooperation Fund, CAS (DNL180310, DNL180308, DNL201912, and DNL201915). The authors acknowledge the Shanghai Synchrotron Radiation Facility (SSRF) for conducting the XANES/EXAFS experiment (BL14W1).

Conflict of Interest

The authors declare no conflict of interest.

Keywords

hollow structures, lithium dendrites, lithium sulfur batteries, nanoreactors, single atoms

Received: July 13, 2020
Revised: August 11, 2020
Published online: August 30, 2020

[1] a) J. W. Choi, D. Aurbach, *Nat. Rev. Mater.* **2016**, *1*, 16013; b) K. Kang, Y. S. Meng, J. Bréger, C. P. Grey, G. Ceder, *Science* **2006**, *311*, 977; c) P. Albertus, S. Babinec, S. Litzelman, A. Newman, *Nat. Energy* **2018**, *3*, 16; d) J. B. Goodenough, Y. Kim, *Chem. Mater.* **2010**, *22*, 587; e) A. Fotouhi, D. J. Auger, K. Propp, S. Longo, M. Wild, *Renewable Sustainable Energy Rev.* **2016**, *56*, 1008; f) X. Chen, W. He, L.-X. Ding, S. Wang, H. Wang, *Energy Environ. Sci.* **2019**, *12*, 938; g) H. Xiang, J. Chen, Z. Li, H. Wang, *J. Power Sources* **2011**, *196*, 8651.

[2] a) P. G. Bruce, S. A. Freunberger, L. J. Hardwick, J.-M. Tarascon, *Nat. Mater.* **2012**, *11*, 19; b) Q. Pang, X. Liang, C. Y. Kwok, L. F. Nazar, *Nat. Energy* **2016**, *1*, 16132; c) X. Shen, H. Liu, X.-B. Cheng, C. Yan, J.-Q. Huang, *Energy Storage Mater.* **2018**, *12*, 161; d) H.-J. Peng, J.-Q. Huang, Q. Zhang, *Chem. Soc. Rev.* **2017**, *46*, 5237.

[3] a) S. S. Zhang, *J. Power Sources* **2013**, *231*, 153; b) R. Xu, J. Lu, K. Amine, *Adv. Energy Mater.* **2015**, *5*, 1500408; c) M. Zhang, W. Chen, L. Xue, Y. Jiao, T. Lei, J. Chu, J. Huang, C. Gong, C. Yan, Y. Yan, *Adv. Energy Mater.* **2020**, *10*, 1903008; d) C. Ye, Y. Jiao, H. Jin, A. D. Slattery, K. Davey, H. Wang, S.-Z. Qiao, *Angew. Chem., Int. Ed.* **2018**, *57*, 16703; e) C. Ye, Y. Jiao, D. Chao, T. Ling, J. Shan, B. Zhang, Q. Gu, K. Davey, H. Wang, S. Z. Qiao, *Adv. Mater.* **2020**, *32*, 1907557; f) C. Ye, D. Chao, J. Shan, H. Li, K. Davey, S.-Z. Qiao, *Matter* **2020**, *2*, 323.

[4] a) D. Lin, Y. Liu, Y. Cui, *Nat. Nanotechnol.* **2017**, *12*, 194; b) X.-B. Cheng, R. Zhang, C.-Z. Zhao, Q. Zhang, *Chem. Rev.* **2017**, *117*, 10403; c) D. Lu, Y. Shao, T. Lozano, W. D. Bennett, G. L. Graff, B. Polzin, J. Zhang, M. H. Engelhard, N. T. Saenz, W. A. Henderson, *Adv. Energy Mater.* **2015**, *5*, 1400993; d) Z. Jiang, S. Wang, X. Chen, W. Yang, X. Yao, X. Hu, Q. Han, H. Wang, *Adv. Mater.* **2020**, *32*, 1906221; e) Z. Jiang, H. Xie, S. Wang, X. Song, X. Yao, H. Wang, *Adv. Energy Mater.* **2018**, *8*, 1801433.

[5] a) Z. Li, H. B. Wu, X. W. D. Lou, *Energy Environ. Sci.* **2016**, *9*, 3061; b) G. Zheng, S. W. Lee, Z. Liang, H.-W. Lee, K. Yan, H. Yao, H. Wang, W. Li, S. Chu, Y. Cui, *Nat. Nanotechnol.* **2014**, *9*, 618; c) M. Chen, Z. Su, K. Jiang, Y. Pan, Y. Zhang, D. Long, *J. Mater. Chem. A* **2019**, *7*, 6250; d) A. Fu, C. Z. Wang, F. Pei, J. Q. Cui, X. L. Fang, N. F. Zheng, *Small* **2019**, *15*, 1804786; e) J. Liu, T. Y. Yang, D.-W. Wang, G. Q. Lu, D. Y. Zhao, S. Z. Qiao, *Nat. Commun.* **2013**, *4*, 2798; f) J. Liu, N. P. Wickramaratne, S. Z. Qiao, M. Jaroniec, *Nat. Mater.* **2015**, *14*, 763.

[6] B. Q. Li, S. Y. Zhang, L. Kong, H. J. Peng, Q. Zhang, *Adv. Mater.* **2018**, *30*, 1707483.

[7] G. Zhou, Y. Zhao, A. Manthiram, *Adv. Energy Mater.* **2015**, *5*, 1402263.

[8] J. Xin, J. Y. Wang, H. R. Lee, K. Yan, Y. Z. Li, F. F. Shi, W. Huang, A. Pei, G. Chen, R. Chen, R. Subbaraman, J. Christensen, Y. Cui, *Sci. Adv.* **2018**, *4*, e1701723.

[9] a) Y. Dong, P. Lu, H. Shi, J. Qin, J. Chen, W. Ren, H.-M. Cheng, Z.-S. Wu, *J. Energy Chem.* **2019**, *36*, 64; b) Y. Zhao, Q. Fu, D. Wang, Q. Pang, Y. Gao, A. Missiul, R. Nemausat, A. Sarapulova, H. Ehrenberg, Y. Wei, G. Chen, *Energy Storage Mater.* **2019**, *18*, 51.

[10] a) L. Ni, G. Zhao, G. Yang, G. Niu, M. Chen, G. Diao, *ACS Appl. Mater. Interfaces* **2017**, *9*, 34793; b) L. Hu, C. Dai, H. Liu, Y. Li, B. Shen, Y. Chen, S.-J. Bao, M. Xu, *Adv. Energy Mater.* **2018**, *8*, 1800709; c) J. He, L. Luo, Y. Chen, A. Manthiram, *Adv. Mater.* **2017**, *29*, 1702707.

[11] a) W. Ren, L. Xu, L. Zhu, X. Wang, X. Ma, D. Wang, *ACS Appl. Mater. Interfaces* **2018**, *10*, 11642; b) D. R. Deng, F. Xue, Y. J. Jia, J. C. Ye, C. D. Bai, M. S. Zheng, Q. F. Dong, *ACS Nano* **2017**, *11*, 6031.

[12] K. Yan, Z. D. Lu, H. W. Lee, F. Xiong, P. C. Hsu, Y. Z. Li, J. Zhao, S. Chu, Y. Cui, *Nat. Energy* **2016**, *1*, 16010.

[13] a) J. Liu, H. Zhang, M. Qiu, Z. Peng, M. K. Leung, W.-F. Lin, J. Xuan, *J. Mater. Chem. A* **2020**, *8*, 2222; b) Y. Chen, S. Ji, C. Chen, Q. Peng, D. Wang, Y. Li, *Joule* **2018**, *2*, 1242; c) H. Zhang, G. Liu, L. Shi, J. Ye, *Adv. Energy Mater.* **2018**, *8*, 1701343.

[14] a) L. Jiao, H.-L. Jiang, *Chem* **2019**, *5*, 786; b) C. Lu, R. Fang, X. Chen, *Adv. Mater.* **2020**, *32*, 1906548; c) Z. Shi, L. Wang, H. Xu, J. Wei,

H. Yue, H. Dong, Y. Yin, S. Yang, *Chem. Commun.* **2019**, *55*, 12056; d) Y. Sun, J. Zhou, H. Ji, J. Liu, T. Qian, C. Yan, *ACS Appl. Mater. Interfaces* **2019**, *11*, 32008.

[15] a) Z. Du, X. Chen, W. Hu, C. Chuang, S. Xie, A. Hu, W. Yan, X. Kong, X. Wu, H. Ji, *J. Am. Chem. Soc.* **2019**, *141*, 3977; b) P. Zhai, T. Wang, W. Yang, S. Cui, P. Zhang, A. Nie, Q. Zhang, Y. Gong, *Adv. Energy Mater.* **2019**, *9*, 1804019; c) Y. Wang, D. Adekoya, J. Sun, T. Tang, H. Qiu, L. Xu, S. Zhang, Y. Hou, *Adv. Funct. Mater.* **2019**, *29*, 1807485; d) G. Zhou, S. Zhao, T. Wang, S. Z. Yang, B. Johannessen, H. Chen, C. Liu, Y. Ye, Y. Wu, Y. Peng, C. Liu, S. P. Jiang, Q. Zhang, Y. Cui, *Nano Lett.* **2020**, *20*, 1252.

[16] J. Xie, B. Q. Li, H. J. Peng, Y. W. Song, M. Zhao, X. Chen, Q. Zhang, J. Q. Huang, *Adv. Mater.* **2019**, *31*, 1903813.

[17] a) K. Xu, M. Zhu, X. Wu, J. Liang, Y. Liu, T. Zhang, Y. Zhu, Y. Qian, *Energy Storage Mater.* **2019**, *23*, 587; b) C. Wang, H. Song, C. Yu, Z. Ullah, Z. Guan, R. Chu, Y. Zhang, L. Zhao, Q. Li, L. Liu, *J. Mater. Chem. A* **2020**, *8*, 3421.

[18] Q. Yang, C. C. Yang, C. H. Lin, H. L. Jiang, *Angew. Chem., Int. Ed.* **2019**, *131*, 3549.

[19] Y.-X. Zhou, Y.-Z. Chen, L. Cao, J. Lu, H.-L. Jiang, *Chem. Commun.* **2015**, *51*, 8292.

[20] W. Cai, G. Li, D. Luo, G. Xiao, S. Zhu, Y. Zhao, Z. Chen, Y. Zhu, Y. Qian, *Adv. Energy Mater.* **2018**, *8*, 1802561.

[21] H. Xu, Q. Jiang, B. Zhang, C. Chen, Z. Lin, *Adv. Mater.* **2020**, *32*, 1906357.

[22] a) F. Y. Fan, W. C. Carter, Y. M. Chiang, *Adv. Mater.* **2015**, *27*, 5203; b) H. Yuan, H.-J. Peng, B.-Q. Li, J. Xie, L. Kong, M. Zhao, X. Chen, J.-Q. Huang, Q. Zhang, *Adv. Energy Mater.* **2019**, *9*, 1802768.

[23] Z. L. Xu, S. Lin, N. Onofrio, L. Zhou, F. Shi, W. Lu, K. Kang, Q. Zhang, S. P. Lau, *Nat. Commun.* **2018**, *9*, 4164.

[24] a) Y. Zhong, L. Yin, P. He, W. Liu, Z. Wu, H. Wang, *J. Am. Chem. Soc.* **2018**, *140*, 1455; b) Y. He, Y. Qiao, Z. Chang, X. Cao, M. Jia, P. He, H. Zhou, *Angew. Chem., Int. Ed.* **2019**, *58*, 11774.

[25] L. Zhang, D. Liu, Z. Muhammad, F. Wan, W. Xie, Y. Wang, L. Song, Z. Niu, J. Chen, *Adv. Mater.* **2019**, *31*, 1903955.

[26] H. Tian, J. Liang, J. Liu, *Adv. Mater.* **2019**, *31*, 1903886.

[27] a) G. Ma, Z. Wen, Q. Wang, C. Shen, J. Jin, X. Wu, *J. Mater. Chem. A* **2014**, *2*, 19355; b) X.-B. Cheng, C. Yan, J.-Q. Huang, P. Li, L. Zhu, L. Zhao, Y. Zhang, W. Zhu, S.-T. Yang, Q. Zhang, *Energy Storage Mater.* **2017**, *6*, 18.

[28] a) H. Shi, C. J. Zhang, P. Lu, Y. Dong, P. Wen, Z.-S. Wu, *ACS Nano* **2019**, *13*, 14308; b) R. Zhang, X. R. Chen, X. Chen, X. B. Cheng, X. Q. Zhang, C. Yan, Q. Zhang, *Angew. Chem., Int. Ed.* **2017**, *56*, 7764.

[29] a) C. Yang, Y. Yao, S. He, H. Xie, E. Hitz, L. Hu, *Adv. Mater.* **2017**, *29*, 1702714; b) J. Pu, J. Li, Z. Shen, C. Zhong, J. Liu, H. Ma, J. Zhu, H. Zhang, P. V. Braun, *Adv. Funct. Mater.* **2018**, *28*, 1804133.

[30] J. He, A. Manthiram, *Adv. Energy Mater.* **2020**, *10*, 1903241.

[31] M.-Q. Zhao, Q. Zhang, J.-Q. Huang, G.-L. Tian, J.-Q. Nie, H.-J. Peng, F. Wei, *Nat. Commun.* **2014**, *5*, 1.

[32] S. Jin, S. Xin, L. Wang, Z. Du, L. Cao, J. Chen, X. Kong, M. Gong, J. Lu, Y. Zhu, *Adv. Mater.* **2016**, *28*, 9094.

[33] X. Zhu, W. Zhao, Y. Song, Q. Li, F. Ding, J. Sun, L. Zhang, Z. Liu, *Adv. Energy Mater.* **2018**, *8*, 1800201.

[34] C. Li, J. Shi, L. Zhu, Y. Zhao, J. Lu, L. Xu, *Nano Res.* **2018**, *11*, 4302.

[35] Z. Yuan, H. J. Peng, J. Q. Huang, X. Y. Liu, D. W. Wang, X. B. Cheng, Q. Zhang, *Adv. Funct. Mater.* **2014**, *24*, 6105.

[36] F. Zhang, Y. Wei, X. Wu, H. Jiang, W. Wang, H. Li, *J. Am. Chem. Soc.* **2014**, *136*, 13963.

[37] G. Eda, G. Fanchini, M. Chhowalla, *Nat. Nanotechnol.* **2008**, *3*, 270.

[38] a) G. Kresse, J. Furthmüller, *Comput. Mater. Sci.* **1996**, *6*, 15; b) G. Kresse, J. Furthmüller, *Phys. Rev. B* **1996**, *54*, 11169.

[39] J. P. Perdew, K. Burke, M. Ernzerhof, *Phys. Rev. Lett.* **1996**, *77*, 3865.

[40] a) G. Kresse, D. Joubert, *Phys. Rev. B* **1999**, *59*, 1758; b) P. E. Blöchl, *Phys. Rev. B* **1994**, *50*, 17953.

[41] G. Henkelman, B. P. Uberuaga, H. J. Jonsson, *Chem. Phys.* **2000**, *113*, 9901.